

# Heat/mass transfer in the slightly unstable atmospheric surface layer

Ann-Sofi Smedman,<sup>a\*</sup> Ulf Högström,<sup>a</sup> J.C.R. Hunt<sup>b,c</sup> and Erik Sahlée<sup>a</sup>

<sup>a</sup> Department of Earth Sciences, Meteorology, Uppsala, Sweden

<sup>b</sup> Department of Earth Sciences, University College, London, UK

<sup>c</sup> JMBurgers Centre, Delft University of Technology, the Netherlands

**ABSTRACT:** In very slightly unstable conditions, when the Obukhov length is much greater than the surface layer depth, it is observed that the structure of the surface layer turbulence does not accord with standard similarity theory. In particular the efficiency of the turbulent exchange of sensible and latent heat is observed to be more strongly enhanced than is consistent with the standard model. Also the profiles of dissipation of turbulent kinetic energy and temperature fluctuation variance are found to depend on the structure of the whole boundary layer (i.e. are non-local), indicating that a large-scale transport process is at work. At the same time, co-spectral analysis shows how the large-scale eddy motions that determine the heat transport process near the surface are typically 1/5 of the surface layer depth. All these features are found to be similar in measurements at a marine site and at a flat land site, indicating that they are determined by the dynamics of the whole boundary layer rather than being simply dependent on the surface boundary conditions.

We hypothesize that in slightly unstable conditions there is a bifurcation in the structure of the large-scale eddy motions. This is a transition from quasi-steady longitudinal roll structures to detached eddies. In the particular regime identified here, the unsteady component dominates the heat transport at the surface. The observed enhancement in the surface layer of the eddy diffusivity of heat is observed to be significantly greater than for momentum. This is shown to be consistent with observations and with a model calculation of the interaction between the surface layer and the descending detached eddies. Copyright © 2007 Royal Meteorological Society

KEY WORDS turbulence mechanism; exchange of sensible heat; marine boundary layer

Received 17 October 2005; Revised 3 October 2006

## 1. Introduction

For conditions with large negative values of the Obukhov length  $L$  (defined in section 2), observations related to the study of heat transfer (sensible and latent) over the sea, presented in the companion paper, Smedman *et al.* (2007) (abbreviated hereafter as SHSJ) have shown features which are not compatible with classical Monin–Obukhov theory (henceforth: MOST). More specifically, it was found in SHSJ from measurements at 10 m above the water surface, that for  $-L > 150$  m, the dimensionless gradient of potential temperature  $\phi_H(z/L)$  reverses its upward trend for decreasing  $-z/L$  into a steep drop, implying a regime with much more efficient heat transfer than expected from MOST. In this paper we show that exactly the same result is found under similar conditions at a flat land site, which indicates that the observed feature is likely to be related to the basic flow regime rather than to some mechanism caused by air/sea interaction. In SHSJ this regime was termed ‘the unstable very close to neutral regime’ or the UVCN regime. Further analysis of the high-quality measurements at the

marine site and at the land site shows that dissipation of turbulent energy and of temperature fluctuations is not in balance with corresponding local production. Analysis of temperature spectra and temperature/vertical velocity co-spectra at the two sites shows a transition of regime, from that dominated by a relatively large scale at moderate instability to the UVCN regime, with an order of magnitude smaller dominant scale. At intermediate stability, ‘camel-shaped’ spectra appear, i.e. spectra with two distinct maxima. This suggests that two turbulent regimes are involved, one dominating at moderate instability and the other in the UVCN regime, and that, in addition, there is an intermediate range where the two regimes coexist. Figure 1(a) and (b) show two flow regimes which might explain the observations: Figure 1(a) shows the well-known situation with longitudinal rolls that cover the entire boundary layer and 1(b) a situation with detached eddies.

The apparent failure of MOST in the UVCN regime calls for an alternative surface layer model for those conditions. In a study of the kinematic structure of the near-neutral atmospheric surface layer (Högström *et al.*, 2002, abbreviated hereafter as HHS), it was demonstrated that a model with detached eddies from above the surface layer impinging on to the surface (Hunt and

\* Correspondence to: Ann-Sofi Smedman, Department of Earth Sciences, Meteorology, Uppsala, Sweden.  
E-mail: ann-sofi.smedman@met.uu.se

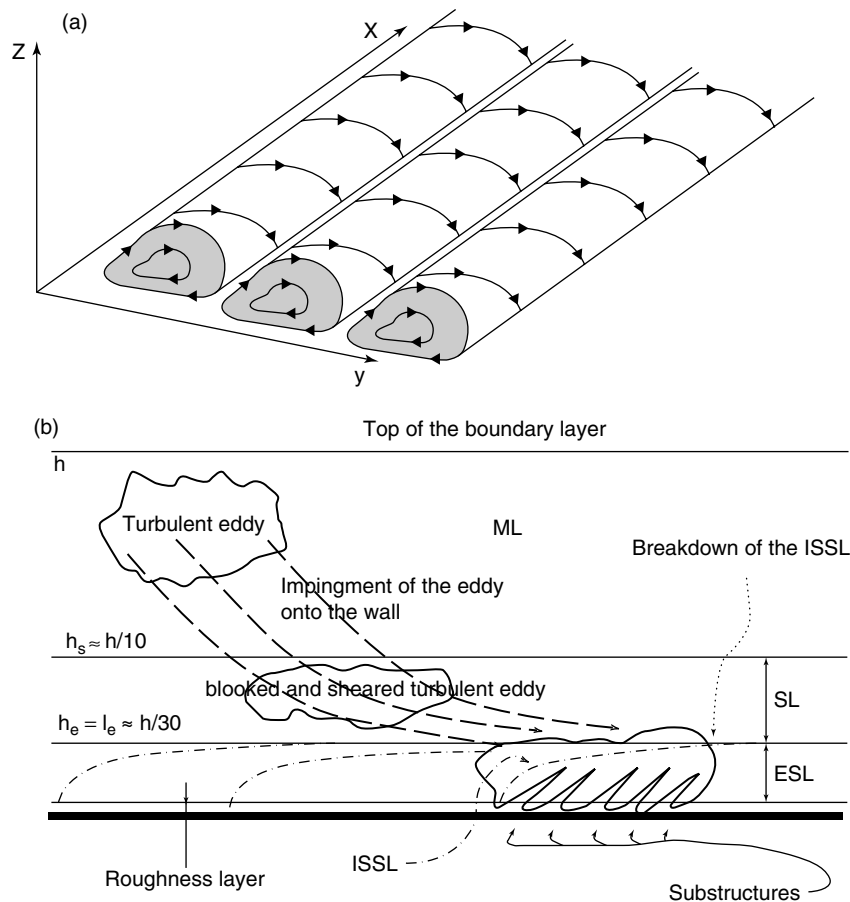


Figure 1. Sketch of two turbulent modes expected to occur in moderate to very slightly unstable conditions at very high Reynolds number. (a) Longitudinal rolls, the mean wind is along the  $x$ -axis; (b) Detached eddies. ISSL = internal shear surface layer; ESL = eddy surface layer; ML = mixed layer. Subfigure (a) adapted from Stull (1988); subfigure (b) from Hunt and Carlotti (2001).

Morrison, 2000) could explain the observed features, cf. Figure 1(b). This is a fundamentally different approach compared to the generally accepted model for neutral boundary layers in typical laboratory conditions (see e.g. Lee *et al.*, 1990; Adrian *et al.*, 2000), which has small eddies being formed right at the surface, growing in size continually with height. In HHS it was argued that the detached eddy model is applicable for high enough turbulent Reynolds number, which is the case in the atmospheric surface layer, but not for typical laboratory conditions and in Direct Numerical Simulations (DNS) of turbulent boundary layers. Thus, the detached eddy model proved successful in explaining the dynamic structure of the near-neutral atmospheric surface layer, but no attempt was made in HHS to test the ability of this model to explain scalar transport phenomena. In this paper we make the hypothesis that the detached-eddy model can be used to explain also the experimental results related to the eddy transport of heat and other scalars.

In section 2, the essentials of MOST are presented. Section 3 presents the two measuring sites and the instrumentation. Results of the analysis are given in section 4, and section 5 contains a theoretical discussion to back up the interpretation of the experimental results. Section 6 gives the conclusions.

## 2. Predictions from Monin–Obukhov theory

The Monin–Obukhov similarity theory (MOST) has been considered the basis of surface layer meteorology since it was first presented in a series of papers about 50 years ago by Obukhov (1946), Monin (1950), and Monin and Obukhov (1953, 1954). The theory essentially predicts that statistical quantities in the surface layer are properly normalized by: (i) the velocity scale  $u_* = \sqrt{(-u'w')_0}$ , where the quantity under the square root sign is the kinematic momentum flux at the surface; (ii) the temperature scale  $T_* = -(\overline{w'\theta'})_0/u_*$ , where  $(\overline{w'\theta'})_0$  is the temperature flux at the surface and (iii) the height above the ground  $z$ , and that the quantities normalized with these parameters are unique functions of the dimensionless height  $z/L$ , where

$$L = -\frac{u_*^3 T_0}{\kappa g (\overline{w'\theta'})_0}, \quad (1)$$

is the Obukhov length, with  $T_0$  = the mean temperature of the surface layer in Kelvin,  $\kappa$  = the von Karman constant, and  $g$  = acceleration of gravity. In this form, the theory is strictly valid for dry air. For moist air, the flux of virtual temperature,  $(\overline{w'\theta'_v})_0$ , replaces  $(\overline{w'\theta'})_0$  in Equation (1) (but not in the definition of  $T_*$ ).

The prediction from MOST for the velocity component variances is:

$$\frac{\sigma_i^2}{u_*^2} = f_i(z/L), \quad (2)$$

where  $i = u, v$  or  $w$  and  $f_i$  are three functions of  $z/L$  only. A consequence of Equation (2) is that the dimensionless variances are all expected to be constants when  $z/L = 0$ , i.e. for neutral stability. As shown in HHS, this prediction is in conflict with results from near-neutral surface layer data, but these data agree well with predictions from the detached-eddy model.

For the velocity component spectra, the general MOST prediction is:

$$\frac{nS_i(n)}{u_*^2} = F_i(z/L, f), \quad (3)$$

where  $F_i$  are separate functions of  $z/L$  and dimensionless frequency  $f = nz/U$  for the  $u$ -,  $v$ - and  $w$ -components respectively.

For the temperature spectrum, the corresponding relation is:

$$\frac{nS_T(n)}{T_*^2} = F_T(z/L, f). \quad (4)$$

An expression similar to (3) is valid for the co-spectrum between  $u$  and  $w$ ,

$$\frac{nC_{\rho_{uw}}(n)}{u_*^2} = G_{uw}(z/L, f), \quad (5)$$

where  $G_{uw}$  is a function of  $z/L$  and  $f$ . Similar expressions apply also for the co-spectrum between  $w$  and  $\theta$  and between  $w$  and  $q$ , where  $q$  is specific humidity.

In accordance with the procedure introduced in Kaimal *et al.* (1972), expressions (3)–(4) are usually normalized in such a way that spectra collapse in the inertial subrange. This means that Equation (3) transforms into:

$$\frac{nS_i(n)}{u_*^2 \varphi_\varepsilon^{2/3}} = F_i'(z/L, f), \quad (3')$$

where  $F_i'$  are three new functions of  $z/L$  and  $f$ . Here,

$$\varphi_\varepsilon = \varepsilon \kappa z / u_*^3 = \varphi_\varepsilon(z/L), \quad (6)$$

where  $\varepsilon$  is the rate of dissipation of kinetic energy and  $\varphi_\varepsilon(z/L)$  is a function of  $z/L$  only.

The expression corresponding to (3') for the temperature spectrum becomes:

$$\frac{nS_T(n)}{T_*^2 \varphi_\varepsilon^{-1/3} \varphi_{NT}} = F_T'(z/L, f), \quad (4')$$

where

$$\varphi_{NT} = \frac{\kappa z N}{T_*^2 u_*}, \quad (7)$$

the dimensionless dissipation of temperature fluctuations, which, according to MOST, is a function only of  $z/L$ , and  $N$  is the rate of dissipation of  $\theta'^2/2$ .

MOST provides relations for the turbulent flux of momentum, temperature and specific humidity and the corresponding mean vertical gradients:

$$\text{for momentum : } \frac{\partial U}{\partial z} \cdot \frac{\kappa z}{u_*} = \phi_m(z/L), \quad (8)$$

$$\text{for temperature : } \frac{\partial \Theta}{\partial z} \cdot \frac{\kappa z}{T_*} = \phi_H(z/L), \quad (9)$$

$$\text{for specific humidity : } \frac{\partial Q}{\partial z} \cdot \frac{\kappa z}{Q_*} = \phi_q(z/L), \quad (10)$$

where  $\Theta$  is mean potential temperature,  $Q$  is mean specific humidity and  $Q_* = (\overline{q'w'})_0/u_*$ , a specific humidity scale.

If the dynamics and thermodynamics are also affected by the mixed layer processes, then these functions also vary with  $h/L$ , where  $h$  is the depth of the boundary layer.

### 3. Measurement sites and instrumentation

#### 3.1. The marine site, Östergarnsholm

This site (located at 57°27'N, 18°59'E) is described in some detail in SHSJ. A map can be found in e.g. Guo Larsén *et al.* (2004). Briefly, atmospheric measurements are performed on a 30 m tower situated at the southern-most tip of a low island. With winds from the sector 80°–220°, shoaling has been shown not to give measurable influence in measured atmospheric parameters for winds at least up to about 15 m s<sup>-1</sup>. Turbulence measurements are performed on a semi-continuous basis with Solent sonic 1012R2 instruments at nominal heights of 10, 17 and 26 m above the water surface. During special intensive measuring campaigns, an MIUU (Meteorological Institute of the University of Uppsala) turbulence instrument has been deployed at 10 m. As discussed in SHSJ, this instrument has far better accuracy and general performance than sonic anemometers, and in the present study only turbulence data obtained with this instrument is used. Slow response, 'profile' measurements of wind and temperature are performed at five levels. Wave characteristics and water temperature is measured onboard a Waverider buoy (owned and run by the Finnish Institute of Marine Research, FIMR), which is moored in 36 m deep water ~4 km from the tower in the direction 115°, representing the wave conditions in the upwind fetch area. Measurements have been performed at the Östergarnsholm site on a semi-continuous basis since May 1995. In SHSJ, data from a period in October 1999 was extensively used. During this period with unstable and neutral conditions, the MIUU instrument was deployed. The same data will be used here.

#### 3.2. The land site, 'Laban's mills'

This site is situated in a flat coastal area on the island of Gotland in the Baltic Sea (57°1.4'N, 18°20'E). Note that only data with wind coming from the land sector are

used here. The vegetation at the site consists of thin grass and herbs which is kept at a height of less than 5 cm by a few cows and horses grazing a vast area, which included the site itself. In the wind sector chosen for the analysis,  $140^\circ$ – $270^\circ$ , this type of vegetation (with some additional scattered low juniper bushes beyond 400 m) extended for more than 2 km upwind. The roughness length for the site calculated from wind profiles is about 1.2 cm. As described in Högström and Bergström (1996), measurements were performed with three turbulence instruments of the MIUU type in three different modes. In the present paper, data from the basic mode will be used. The turbulence instruments were then placed on a slim triangular mast at 1.6 m, 3.1 m and 6.3 m above the surface respectively. In addition, slow response measurements of wind and temperature were made at five levels from about 0.3 m to about 6 m above the surface.

The measurements at this site were performed during late June and July 1991 and happened to include extensive periods with relatively strong winds, in the range  $7$ – $10 \text{ m s}^{-1}$ , so that near neutral conditions occur frequently in the dataset.

## 4. Results of the data analysis

### 4.1. Data selection

Data have been chosen from the two sites that cover a wide range of unstable and near-neutral conditions, right up to  $z/L = 0$ . For simplicity, the Östergarnsholm site will henceforth be denoted ‘the marine site’ and the Laban’s mills site ‘the land site’. The interest here is primarily on data from the near-neutral range, but the more unstable data are needed in order to determine the limits of validity for MOST.

From the land site, data were chosen from two situations: (i) 20 June 1991, eight half-hour runs, representing typical unstable conditions; (ii) 16 July 1991, 17 h – 20 h and 21 July 1991, 06 h – 11 h, representing two periods with large negative  $L$ -values. Note that, because of prevailing relatively strong winds, both near-neutral situations can be regarded as quasi-stationary.

Most of the data from the marine site come from a period in October 1999 when the MIUU instrument was deployed and conditions were ideal for the present study, giving a wide range of wind speed (from  $3 \text{ m s}^{-1}$  to about  $14 \text{ m s}^{-1}$ ) and with  $L$  ranging from about  $-10 \text{ m}$  to  $-300 \text{ m}$ . This dataset consists of 66 one-hour mean values.

### 4.2. $\phi_m$ , $\phi_H$ , $\phi_\varepsilon$ and $\phi_{NT}$

A plot of the dimensionless wind gradient,  $\phi_m$ , at the land site (not shown here) shows that data from the three measuring levels 1.6, 3.1 and 6.3 m scatter without any bias around the curve suggested by Högström (1988) in the stability range  $-1 < z/L < 0$ :

$$\phi_m = (1 - 19 z/L)^{-1/4}. \quad (11)$$

In the range  $-0.01 < z/L < 0$ , there are seven data points, with mean  $z/L = -0.005$  and mean  $\phi_m = 0.963$ , which is within experimental accuracy of the corresponding value from Equation (11), 0.977.

Data related to the near-neutral wind profile at the marine site have been thoroughly treated in Smedman *et al.* (2003). It was shown that the shape of the neutral wind profile depends on the sea state. Only in conditions with pure wind sea, defined as  $E_1/E_2 < 0.2$ , where  $E_1$  is the energy of waves travelling faster than the 10 m wind (swell) and  $E_2$  is the corresponding energy of the waves travelling slower than the wind (local waves), a truly logarithmic wind profile is found. Because of the complicated interaction of the wind profile with the wave field, no attempt has been made so far to determine  $\phi_m$  for all conditions. It is, however, clear that in neutral air and pure wind sea conditions,  $\phi_m = 1.0$ .

Figure 10 in SHSJ shows a plot of  $\phi_H$  against  $z/L$  for the 10 m level at the marine site. In the range  $-2 < z/L < -0.1$ , the data points are seen to follow the trend of the curve suggested by Högström (1988):

$$\phi_H = 0.95(1 - 11.6 z/L)^{-1/2}. \quad (12)$$

For  $-z/L < 0.1$ , most points deviate strongly downwards. All those data have  $-L > 150 \text{ m}$ . Note that this feature, which is so clear in the 10 m plot, is entirely absent in the corresponding plot of  $\phi_H$  for 17 and 26 m height, Figure 11 of SHSJ.

In Figure 2,  $\phi_H$  from the land site has been plotted against  $z/L$ . Data from the three heights (see legend) all follow Equation (12) well from  $z/L = -1$  to  $z/L \approx -0.03$ , from where the data points start to drop dramatically. Examination of the individual data reveals that transition from the MOST mode, represented by Equation (12), to a mode with much smaller  $\phi_H$ -values occurs for  $-L \approx 150 \text{ m}$ , just as observed at the marine site.

The dimensionless dissipation  $\phi_\varepsilon$  has been derived from inertial subrange spectra. Thus, according to the

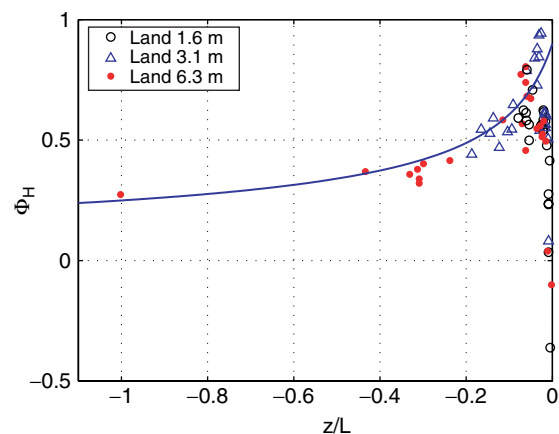


Figure 2. Dimensionless temperature gradient  $\phi_H$  plotted against  $z/L$ . Data from the land site, at three heights, according to legend. This figure is available in colour online at [www.interscience.wiley.com/qj](http://www.interscience.wiley.com/qj)

Kolmogoroff theory for the inertial subrange, the spectrum of vertical velocity in this range is:

$$\frac{nS_w(n)}{u_*^2} = \frac{\alpha_3}{(2\pi\kappa)^{2/3}} \phi_\varepsilon^{2/3} f^{-2/3}, \quad (13)$$

where  $\alpha_3$  is the transverse Kolmogoroff constant = 0.69. An analogous expression is obtained for the longitudinal component, but with the longitudinal Kolmogoroff constant  $\alpha_1 = (3/4) \cdot 0.69 = 0.52$  replacing  $\alpha_3$ . It is evident from the spectral graphs shown later that an extended  $-2/3$  range is observed in the  $u$ - and  $w$ -spectra from both sites and also that the  $3/4$  ratio requirement for local isotropy is met to within measurement accuracy.

Figure 3 shows a composite plot of  $\phi_\varepsilon$ -data against  $z/L$  for both sites, together with two curves which represent results from previous surface-layer experiments, the one denoted 'Kansas' is from Wyngaard and Coté (1971), and the one denoted 'UH' from Högström (1990). The data points denoted 'sea' are from the marine site, 10 m; the remaining symbols represent 1.6 and 6.3 m data from the land site (see legend). The points appear to follow the line denoted 'UH' roughly within the range  $-1.8 < z/L < -0.3$ , but for  $-z/L < 0.3$  they separate clearly according to height: the 'sea' 10 m data and the 6.3 m land data appear to be as low as 0.5 for  $z/L = 0$ , whereas the corresponding 1.6 m data from the land site are in the range 1.5–2.5. This means that local dissipation is not equal to local production at any of the heights shown (which would give  $\phi_\varepsilon = 1.0$ ) in neutral conditions. Since the measurements – at least in the mean – represent nearly steady conditions with zero horizontal advection, it is reasonable to conclude that turbulent energy is being brought down from layers in the height range 6–10 m (and probably higher up) and down to very close to the surface, where dissipation exceeds local production.

Analysis of atmospheric data has clearly demonstrated (e.g. Kaimal *et al.*, 1972; see also Sreenivasan, 1996)

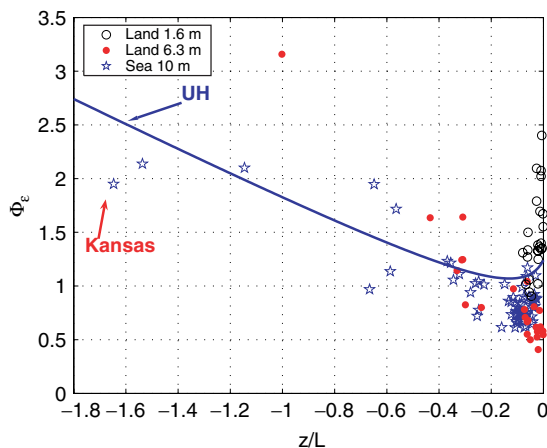


Figure 3. Dimensionless dissipation  $\phi_\varepsilon$  plotted against  $z/L$ . Data from the marine site, 10 m and from the land site, 1.6 and 6.3 m above the ground. Curve denoted 'Kansas' is from Kaimal *et al.* (1972) and 'UH' is from Högström (1990). This figure is available in colour online at [www.interscience.wiley.com/qj](http://www.interscience.wiley.com/qj)

that temperature spectra in the surface layer have an extended high-frequency  $-5/3$  region. It has traditionally been assumed that this is related to the existence of a 'convective inertial subrange', as first suggested by Corrsin (1951), implying that the small-scale temperature fluctuation field is locally isotropic and that there indeed exists a cascade of temperature fluctuations from larger to smaller scales in this spectral range. The Corrsin (1951) prediction for this spectral range is

$$F_\theta(k_1) = \beta_1 \varepsilon^{-1/3} N k_1^{-5/3}, \quad (14)$$

where  $\beta_1$  is a constant analogous to  $\alpha_3$  in Equation (13) and  $k_1$  is longitudinal wave number  $\approx 2\pi n/U$ . In the normalized form (4'), Equation (14) can be written:

$$\frac{nS_\theta(n)}{T_*^2 \phi_{NT} \phi_\varepsilon^{-1/3}} = \frac{\beta_1}{(2\pi\kappa)^{2/3}} f^{-2/3}. \quad (15)$$

As convincingly demonstrated by Warhaft (2000), the small-scale temperature fluctuation field is, however, far from locally isotropic. Nevertheless, atmospheric surface layer data show that Equation (15), with  $\beta_1 \approx 0.8$  (Sreenivasan, 1996), appears to have 'universal' validity. The balance equation for  $\overline{\theta'^2}/2$  during stationary and horizontally homogeneous conditions has the following normalized form:

$$\phi_H - \frac{\kappa z}{u_* T_*^2} \frac{1}{2} \frac{\partial \overline{w'\theta'^2}}{\partial z} - \phi_{NT} = 0, \quad (16)$$

where the first term is the dimensionless production of temperature fluctuations from mean gradient–temperature flux interaction, the middle term the dimensionless rate of turbulent transport of temperature variance and the last term is the dimensionless dissipation of temperature fluctuations. Results from several surface layer experiments (Wyngaard and Coté, 1971; Högström, 1990) have shown that, for a wide range of conditions, the transport term is much smaller than the other two terms of Equation (16), so that

$$\phi_{NT} \approx \phi_H. \quad (16')$$

Figure 4 shows  $\phi_{NT}$  calculated from normalized high-frequency temperature spectra with Equation (15), assuming  $\beta_1 = 0.8$ , plotted against  $z/L$ . Data are from 1.6 and 6.3 m at the land site and from 10 m at the marine site, see legend. Also plotted is the  $\phi_H$  curve from Högström (1988), Equation (12).

The data from the land site are seen to scatter around this curve without noticeable bias down to  $-z/L$ -values as low as 0.01, but for even smaller values,  $\phi_{NT}$  attains values in the range 1.5–2.5. Note that in this range, which is identical to the UVCN range, the actual  $\phi_H$ -values are observed not to follow Equation (12) but to decrease towards zero, Figure 2, making the difference between  $\phi_{NT}$  and  $\phi_H$ , i.e. the middle term of Equation (16), very large. With accurate enough measurement of  $\overline{w'\theta'^2}$  at several levels, it is, in principle, possible to calculate the

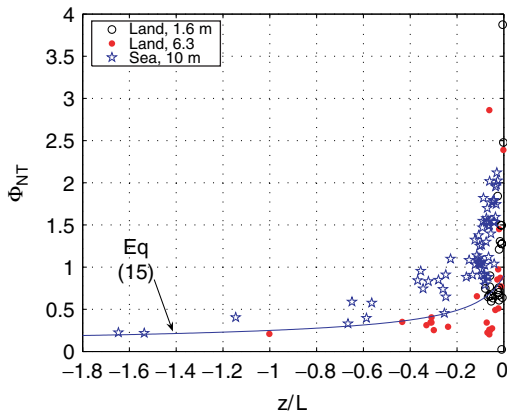


Figure 4. Dimensionless dissipation of temperature fluctuations  $\phi_{NT}$  plotted against  $z/L$ . Data from the land site 1.6 and 6.3 m and from the marine site 10 m. Symbols according to legend. The curve represents the expression for  $\phi_H$ , Equation (15). This figure is available in colour online at [www.interscience.wiley.com/qj](http://www.interscience.wiley.com/qj)

transport term directly by making a polynomial best fit to the data, and taking the derivative at appropriate levels. Apart from the inherent large scatter of estimates of third-order moments, there is a considerable uncertainty in the gradient at the heights of 1.6 and 6.3 m derived from a second-order best fit to measurements at 1.6, 3.1 and 6.3 m. Nevertheless, fair agreement in the mean is obtained between the term  $-\left[\kappa z/2(u_* T_*^2)\right]\partial(w'\theta^2)/\partial z$  obtained with this method and  $\phi_{NT} - \phi_H$ , albeit with great scatter (not shown).

The data from *the marine site* in Figure 4 are in reasonable agreement with the curve representing Equation (12) up to  $-z/L \approx 0.3$ , where  $\phi_{NT}$  starts to be systematically larger than  $\phi_H$ . For  $-z/L$ -values below about 0.1,  $\phi_{NT}$  rises sharply, being in the range 1–2 for  $-z/L < 0.07$ , i.e. for  $-L > 150$  m, which is the range where  $\phi_H$  is observed to decrease sharply. Thus, a similar general pattern of imbalance between local production and dissipation in the UVCN range as found at the land site is observed at the marine site.

### 4.3. Spectral analysis

In order to get a better understanding of the turbulence processes in the UVCN range, spectral and co-spectral analysis have been employed. There appears to be very few previous studies of spectra for very close to neutral stationary conditions, except those shown in HHS, but they do not include temperature spectra and  $w\theta$  co-spectra.

It is, however, appropriate to start this study by looking at more unstable cases, which have been extensively studied in the past. Plots have been made of the spectra for the velocity components and for temperature based on data from both the marine site and the land site. For wind component spectra, normalized estimates according to Equation (3') have been plotted against dimensionless frequency  $f$ . These plots (not shown here) are very similar to the corresponding plots in Kaimal *et al.* (1972).

For the corresponding temperature spectrum, the normalization (4') has been used. Figure 5 shows the result for the land site. In agreement with predictions from MOST and the Kolmogoroff theory, data from 1.6 m and 6.3 m are seen to collapse very closely in the inertial subrange ( $f > c. 0.5$ ). Data are also fairly close together in the intermediate frequency range,  $10^{-2} < f < 0.5$ , with spectral maximum at  $f \approx 10^{-2}$ . In contrast, for  $f < 10^{-2}$ , the spectral estimates scatter over a decade for any  $f$ . This is in complete agreement with the corresponding result in Kaimal *et al.* (1972). At the time of that publication, the authors had no explanation for this feature. Today it is known that the scatter in this frequency range is the result of boundary-layer scale eddies, which introduce a scaling with  $h/L$ , where  $h$  is the height of the boundary layer (cf. e.g. Johansson *et al.*, 2001).

Figure 6 shows an example of spectra for the longitudinal wind component  $u$ , for the vertical velocity  $w$  and for temperature  $T$  at 1.6 m from a typical unstable

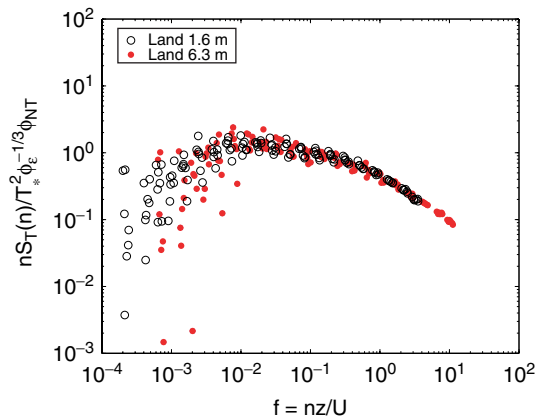


Figure 5. Typical dimensionless temperature spectra for unstable conditions ( $L \approx -30$  m) at the land site plotted against dimensionless frequency,  $f = nz/U$ . This figure is available in colour online at [www.interscience.wiley.com/qj](http://www.interscience.wiley.com/qj)

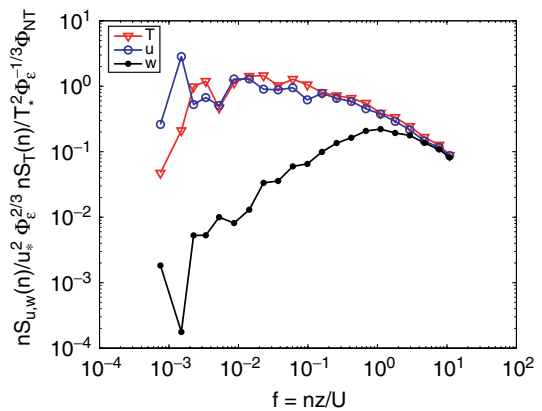


Figure 6. Examples of unstable ( $L = -14$  m) dimensionless spectra for the longitudinal wind component, the vertical wind component and temperature from the land site, 1.6 m, plotted against dimensionless frequency,  $f = nz/U$ . This figure is available in colour online at [www.interscience.wiley.com/qj](http://www.interscience.wiley.com/qj)

case at the land site (in this particular case,  $L = -14$  m). Note, that the  $u$ - and  $T$ -curves follow each other closely, with a shallow maximum at  $f \approx 10^{-2}$ . The  $w$ -spectrum contrasts strongly, with maximum at  $f \approx 1$ .

Figure 7 illustrates how the dimensionless temperature spectrum at the marine site develops as the Obukhov length changes from  $-10$  m to  $-240$  m. Each spectrum in the graph is a mean based on 3 to 10 hours of measurement. For  $L = -10$  m, curve with dots, a spectrum of the type shown in Figure 5 ensues, having a maximum around  $f \approx 2 \cdot 10^{-2}$ . For  $L = -42$  m, curve with triangles, the spectrum has two distinct maxima: a low-frequency peak at  $f \approx 10^{-2}$  and a secondary peak of slightly lower magnitude at  $f \approx 0.4$ . For  $L = -145$  m, curve with stars, this pattern is preserved, but note that for this category, the spectral magnitude at  $f \approx 0.4$  is about 40% higher than the corresponding magnitude of the low-frequency spectrum. The fourth spectrum, curve with open circles, represents a mean  $L = -240$  m. This spectrum (which is based on 10 hours of measurements) exhibits one, very prominent maximum at  $f \approx 0.2$ . Figure 8 shows spectra of  $u$ ,  $w$  and temperature for a case with  $L = -385$  m at the marine site. Comparing the spectral curves of this plot with the corresponding curves in the plot for the case with  $L = -14$  m, Figure 6, illustrates the dramatic change in the temperature spectrum which occurs for this change of  $L$ . From being very similar to the  $u$ -spectrum at  $L = -14$  m, the temperature spectrum very nearly attains the form of the  $w$ -spectrum for  $L = -385$  m.

A similar transition of the temperature spectra with increasing  $-L$  as that observed at the marine site is also found at the land site (not shown here). For the UVCN regime, i.e. for  $-L > 150$  m, temperature spectra over land and over the sea are remarkably similar for  $f > 10^{-2}$ . This is illustrated in Figure 9, which shows, as a typical example, one spectrum from the land site and one from the marine site with similar  $L$ -values (around  $-300$  m). Note that the low-frequency points are very

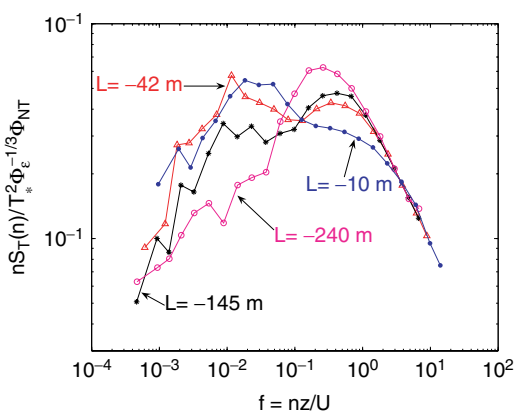


Figure 7. Mean normalized temperature spectra from the marine site for four groups of data, plotted against dimensionless frequency,  $f = nz/U$ , representing mean  $L$ -values of  $-10$  m,  $-42$  m,  $-145$  m and  $-240$  m respectively. Each curve is the mean of 3 to 10 hours of measurement. This figure is available in colour online at [www.interscience.wiley.com/qj](http://www.interscience.wiley.com/qj)

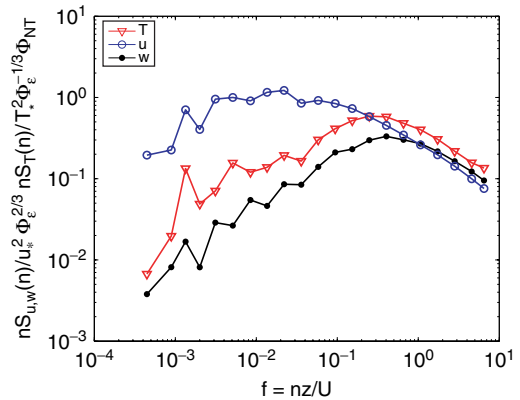


Figure 8. Examples of dimensionless spectra in the UVCN-range ( $L = -385$  m) for the longitudinal wind component, the vertical wind component and temperature from the marine site, 10 m, plotted against dimensionless frequency,  $f = nz/U$ . This figure is available in colour online at [www.interscience.wiley.com/qj](http://www.interscience.wiley.com/qj)

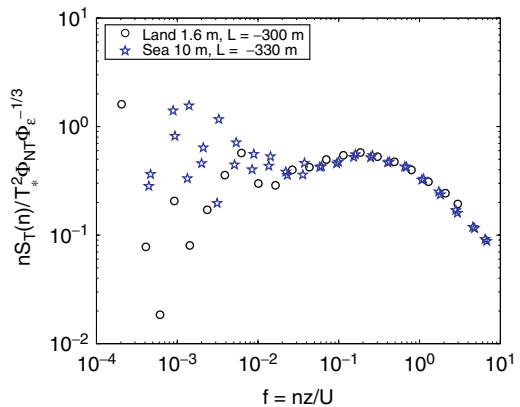


Figure 9. Examples of dimensionless temperature spectra in the UVCN-range at the land site, 1.6 m ( $L = -330$  m), and at the marine site, 10 m ( $L = -330$  m), plotted against dimensionless frequency,  $f = nz/U$ . This figure is available in colour online at [www.interscience.wiley.com/qj](http://www.interscience.wiley.com/qj)

scattered in this graph. This is probably mainly a result of limited statistical representativity in this frequency range (cf. Figure 5 of Smedman *et al.*, 2003).

The scale of the transport process is most directly studied in a co-spectral analysis. The following graphs show co-spectra divided by total co-variance plotted against dimensionless frequency  $f$ . Mean  $w\theta$  co-spectra from the marine site have been derived for the same four groups of  $L$  as used for the analysis of the temperature spectra in Figure 7 and are plotted in Figure 10. The progression of the co-spectral curves with increasing  $-L$  is qualitatively similar to that of the corresponding temperature spectra. For the case with  $L = -10$  m, a single peak in the co-spectrum is found at  $f \approx 3 \cdot 10^{-2}$ . With increasing  $-L$ , this maximum decreases in magnitude at the same time as a high-frequency maximum gradually builds up near  $f \approx 0.3$ . For the case of  $L = -240$  m, nothing is left of the low-frequency maximum and the high-frequency peak is very prominent. This again, is a very significant signature of the UVCN regime. Figure 11 illustrates how a very similar development of  $w\theta$  co-spectra with  $L$  occurs

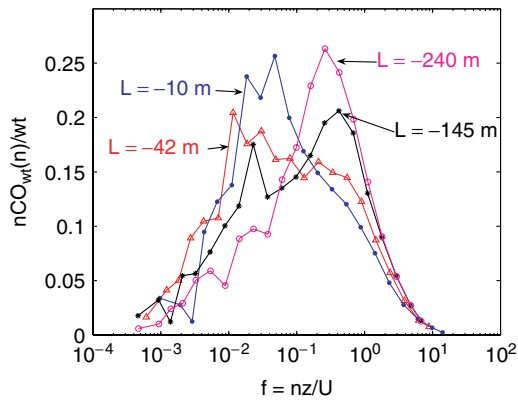


Figure 10. Mean normalized  $w\theta$  co-spectra from the marine site for four groups of data, plotted against dimensionless frequency,  $f = nz/U$ , representing mean  $L$ -values of  $-10$  m,  $-42$  m,  $-145$  m and  $-240$  m respectively. Each curve is the mean of 3 to 10 hours of measurement. This figure is available in colour online at [www.interscience.wiley.com/qj](http://www.interscience.wiley.com/qj)

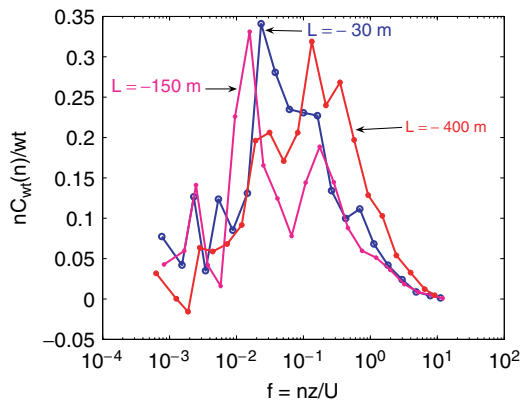


Figure 11. Same as Figure 10, but from 6.3 m at the land site. Each curve is based on just one 30-minute run. This figure is available in colour online at [www.interscience.wiley.com/qj](http://www.interscience.wiley.com/qj)

at the land site, i.e. for  $L = -30$  m a single maximum at  $f \approx 2 \cdot 10^{-2}$  occurs; for  $L = -150$  m the curve has two peaks, one near  $f \approx 2 \cdot 10^{-2}$  and one at around  $f \approx 0.2$ ; for  $L = -400$  m, the corresponding curve has only one maximum, at  $f \approx 0.1$ . The curves in the 'land plot', Figure 11, are more ragged than those in the corresponding 'marine plot', Figure 10, but this mainly reflects the fact that each curve in the 'land plot' is based on only one 30 minute run, whereas each of the curves in the 'marine plot' is the mean of 3–10 such runs.

In Figure 12 a co-spectral comparison is made, for  $w\theta$  in subplots (a) and (b), and for  $uw$  in subplots (c) and (d). Subplots in the first column, (a) and (c), are from the land site and in the second column, (b) and (d), from the marine site. In each subplot, there is one curve representing moderately convective conditions,  $-L < 50$  m, and one representing the UVCN range,  $-L > 150$  m. From a comparison of the  $w\theta$  subplots, (a) and (b), it is seen that a closely similar change of non-dimensional frequency for co-spectral maximum  $f_{\max}$  is found at the land site and at the marine site. This

contrasts strongly with the corresponding plots for the  $uw$  cospectra, (c) and (d), where an insignificant change of  $f_{\max}$  is observed both at the land site and at the marine site.

#### 4.4. Quadrant analysis

Quadrant analysis is a conditional sampling technique originally developed for turbulent laboratory flows by Lu and Willmarth (1973). It separates the flux into four categories, according to the sign of the two fluctuating components. Thus, with the two components denoted  $x$  and  $y$  and numbering the quadrants according to mathematical convention, we have for the  $x - y$  plane:

quadrant I	$x > 0, y > 0$
quadrant II	$x < 0, y > 0$
quadrant III	$x < 0, y < 0$
quadrant IV	$x > 0, y < 0$ ,

where  $y = w$  and  $x = \theta$  in our case. For the heat flux,  $\overline{w'\theta'}$ , quadrants I and III give positive contributions, warm air being transported upward for quadrant I and cold air downward for quadrant III.

The importance of relatively short-lived large values of the moments  $x'y'$  may be seen by estimating the contribution of these events to the total flux and by comparing this with the fraction of time these large values occur. This is accomplished by determining the cumulative frequency distributions of the fluxes when keeping values larger than some given fraction of the average flux. This is equivalent to using the hyperbolic hole introduced by Willmarth and Lu (1974). The size  $H$  of the hole is defined as

$$H = |x'y'| / \overline{|x'y'|}, \quad (17)$$

where the point  $(x', y')$  lies on the hyperbola which bounds the whole region in the  $x - y$  plane. The hyperbolic hole is defined as the shaded area in Figure 13 and becomes an excluded region in the quadrant analysis. By progressively increasing the magnitude of  $H$ , the importance of events exhibiting increasingly large values of  $|x'y'|$  can be determined within each quadrant.

Following Raupach (1981), a flux fraction  $S_{iH}$ , where subscript  $i$  refer to the quadrant number, is defined as

$$S_{iH} = [x'y']_{iH} / \overline{|x'y'|}, \quad (18)$$

where the brackets signify a conditional average. This conditional average is formally defined using a conditioning function  $I_{iH}$  which obeys

$$I_{iH} = 1, \text{ if the point lies in the } i\text{-th quadrant and} \\ |x'y'| \geq H \overline{|x'y'|} \\ = 0 \text{ otherwise.}$$

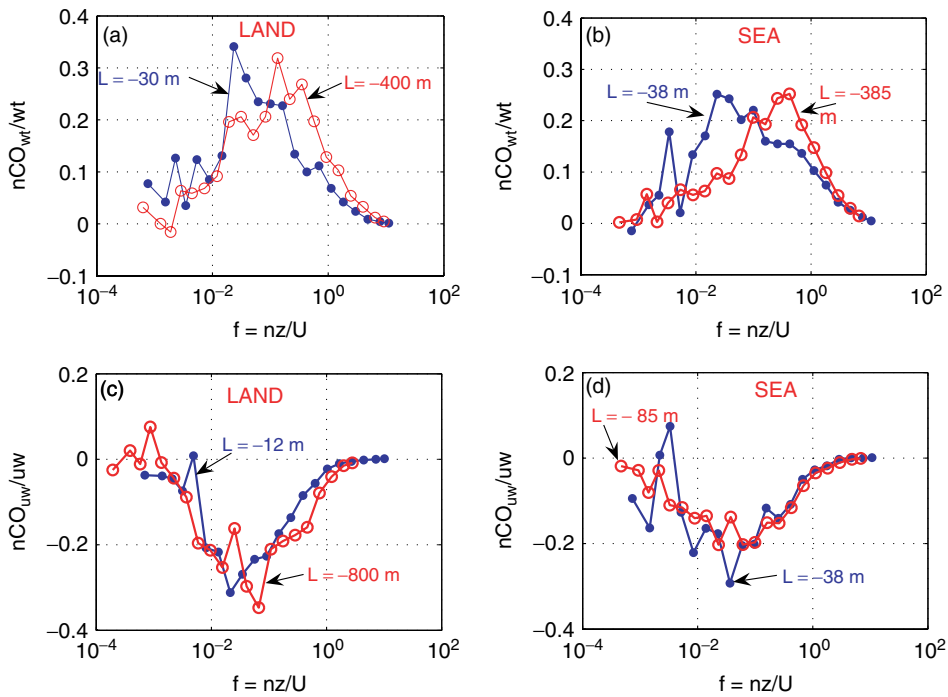


Figure 12. Examples of dimensionless co-spectra plotted against dimensionless frequency,  $f = nz/U$ , for  $w\theta$ , subplots (a) and (b) and for  $wu$ , subplots (c) and (d). Subplots (a) and (c) are from the land site, subplots (b) and (d) from the marine site. In each subplot there is one curve for unstable conditions ( $-12\text{ m} > L > -38\text{ m}$ ) and one for the UVCN range ( $-385\text{ m} > L > -800\text{ m}$ ). This figure is available in colour online at [www.interscience.wiley.com/qj](http://www.interscience.wiley.com/qj)

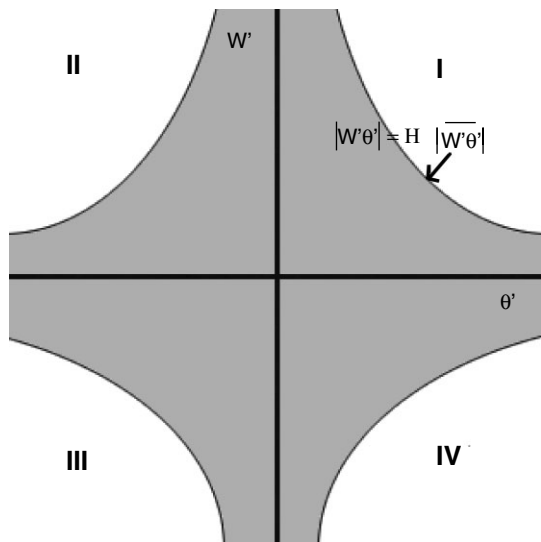


Figure 13. Temperature and vertical velocity fluctuation domain showing the quadrants and the hyperbolic excluded region (hatched area).  $H$  is size of the hyperbolic hole.

Then the conditionally averaged flux becomes

$$[x'y']_{iH} = \liminf \frac{1}{T} \int_0^T x'y'(t) I_{iH}(t) dt. \quad (19)$$

Since the flux fractions are normalized quantities, it is clear that

$$\sum_{i=1}^4 S_{i,0} = 1. \quad (20)$$

Figure 14(a) and (b) shows examples of the cumulative distributions in the four quadrants for  $\overline{w'\theta'}$  for 10 m at the marine site. Figure 14(a) is from a moderately unstable case, with  $L = -6.3\text{ m}$ ,  $U_{10} = 4.9\text{ m s}^{-1}$  and sea/air temperature difference  $\Theta_w - \Theta_{10} = 5.0\text{ K}$  (21 October, 1230h), and Figure 14(b) from a typical UVCN-case (23 October, 1730h), with  $L = -292\text{ m}$ ,  $U_{10} = 12.5\text{ m s}^{-1}$  and  $\Theta_w - \Theta_{10} = 1.3\text{ K}$ . Note that  $H$ , by definition, is always positive. For the composite quadrant plots of Figure 14(a) and (b) this implies that  $H$  increases from the centre line towards the right for quadrants I and IV and towards the left for quadrants II and III. Note also that the heat flux fractions  $S_{iH}$  (Figure 14(a) and (b)) are positive for quadrants I and III and negative for quadrants II and IV.

Figure 14(a) is a good example, which shows the heat flux analysis for the moderately convective case. By extracting first the heat flux fraction values for the various quadrants for hole size  $H = 0$ , then  $S_{1,0} = 0.70$ ,  $S_{2,0} = -0.07$ ,  $S_{3,0} = 0.45$ ,  $S_{4,0} = -0.08$ , the sum of which is 1.0, in accordance with Equation (20). For  $H = 5$ , the corresponding approximate figures are:  $S_{1,5} = 0.39$ ,  $S_{2,5} = -0.00$ ,  $S_{3,5} = 0.02$ ,  $S_{4,5} = -0.01$ , the sum of which is 0.40, meaning that 40% of the flux occurs in events where the flux is more than five times the average value. Evaluating the corresponding flux fractions from the graph for the UVCN case, Figure 14(b), for  $H = 5$ , gives the following numbers:  $S_{1,5} = 0.35$ ,  $S_{2,5} = -0.02$ ,  $S_{3,5} = 0.26$ ,  $S_{4,5} = -0.03$ , the sum of which is 0.56. Here 56% of the flux occurs in events whose flux magnitude is more than five times the average flux.

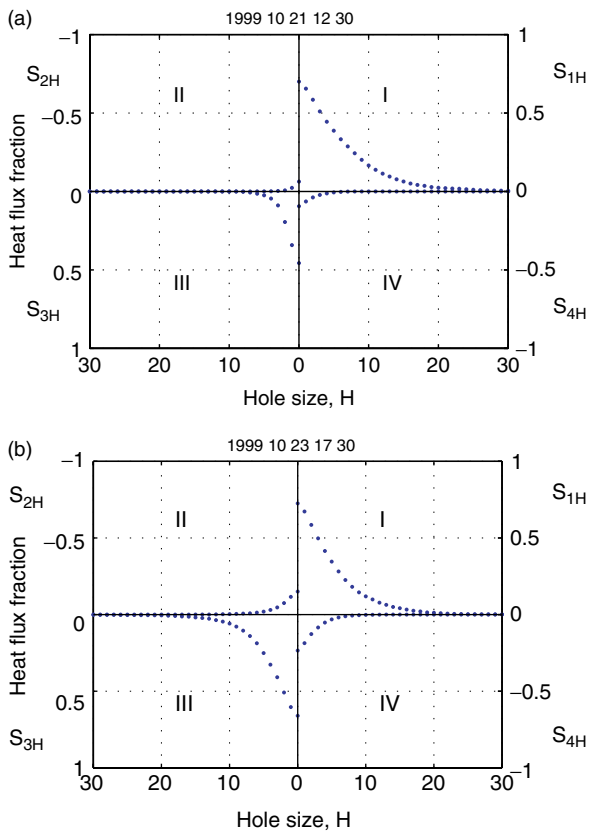


Figure 14. Examples of quadrant analysis from the marine site, 10 m for the heat flux. Subplot (a) represents a situation with moderate convection ( $L = -6.3$  m,  $U_{10} = 4.9$  m s<sup>-1</sup>,  $\Theta_w - \Theta_{10} = 5.0$  K), and subplot (b) a UVCN case ( $L = -292$  m,  $U_{10} = 12.5$  m s<sup>-1</sup>,  $\Theta_w - \Theta_{10} = 1.3$  K). The subplots give flux fractions  $S_{iH}$ , Equation (21) as function of hole size  $H$ , Equation (20), in each of four quadrants. Note, that  $H$ , by definition, is positive for each quadrant and that the sign of  $S_{iH}$  is positive for quadrants I and III and negative for quadrants II and IV. This figure is available in colour online at [www.interscience.wiley.com/qj](http://www.interscience.wiley.com/qj)

A comparison of Figure 14(a) for the moderately unstable case and 14(b) for the UVCN case shows upward transfer of temperature excess (quadrant I events) to dominates the heat flux in the moderately unstable case (Figure 14a), whereas in the UVCN case (Figure 14(b)), downward transport of temperature deficit (quadrant III events) is almost equally important for the heat transport process. The relevance of the observed change in the heat flux regime is discussed in the next section.

## 5. Discussion

### 5.1. Theoretical considerations

In the analysis of HHS the flow properties were found to be quite insensitive to the sign of  $z/L$ , i.e. the functions are smooth and continuous and the results valid for  $-\delta < z/L < \delta$ , where  $\delta \propto O(0.1)$ . However observations (Guo Larsén *et al.*, 2004) show that this is not the case for the exchange of sensible heat at the marine site. They indicate a discontinuity of  $C_{HN}$  at  $z/L = 0$ . Thus, the heat exchange mechanism is clearly different for  $z/L = +0$

and  $-0$ . In the present study, we focus on the latter regime.

It is well established from experimental and theoretical studies (e.g. Mason and Sykes, 1982) that for slightly unstable atmospheric boundary layers longitudinal roll structures exist that extend vertically throughout the entire boundary layer, see Figure 1(a). Khanna and Brasseur (1998) demonstrated in a Large Eddy Simulation study (LES) for a case with  $h/L = -0.44$  the appearance of typical roll structures. For this case, simulated temperature spectra coincide closely with corresponding spectra for the longitudinal wind component – just as seen in our Figure 6. The longitudinal roll model does, however, not explain the transition of the temperature spectra that we observe for the UVCN regime, Figure 8. A more complex model is required that describes the nature of the transition to this type of eddy structure.

It was demonstrated in HHS that the detached-eddy model (Townsend, 1976; Hunt and Morrison, 2000), Figure 1(b), describes the large-scale motions in the near-neutral atmospheric surface layer. No predictions were, however, given in HHS for the turbulent exchange of heat and matter or for the effects of weak buoyancy.

In the absence of the shear roll structures, the largest scale detached eddies above the surface layer have characteristic sheared forms with horseshoe structures of vortex lines (e.g. Adrian *et al.*, 2000). The transition from this kind of large-scale flow to the quasi-steady form of roll structures, Figure 1(a), corresponds to the general pattern of behaviours in many dynamical systems. The rolls are a ‘bistable’ form, since at any point the flow can be up or down. (e.g. Holmes *et al.*, 1996). This transition has some similarities to the steady/unsteady behaviour of the roll/shear structures in Taylor Couette flow (Benjamin, 1978).

This conceptual framework indicates how the near-neutral atmospheric boundary layer might change with weak buoyancy forces. Since, by hypothesis, the eddy structure changes throughout the depth of the layer, it would follow that surface scaling cannot provide a complete description for the changes that are observed. Furthermore, since the change in structure could be in the form of a bifurcation, this suggests that the change in the boundary layer structure may occur at a critical value of  $h/L$ . Since we have no measurements of the boundary layer height  $h$  in the present study, we implicitly assume a constant value for this parameter and formulate a criterion for the UVCN regime in terms of a limiting value for  $L = -150$  m, as already noted.

Figure 1(b) illustrates schematically the situation in the case when detached eddies dominate. A turbulent eddy coming from above is seen to undergo blocking and shearing when entering the surface layer. As the eddy contacts the surface it is strongly deformed, extending itself over a long distance – which is, in fact, of the same order as the depth of the boundary layer, i.e. typically several hundred metres. But its depth is only about 1/30 of the boundary layer, i.e. 10–30 m. In the strong shear close to the surface, small-scale turbulent substructures

are formed by the mean shear and within the eddies. The detached eddies are locally produced in the outer parts of the boundary layer by a similar mechanism as those in a free shear layer.

A necessary requirement for the detached-eddy mechanism to be effective is that the turbulent Reynolds number  $Re_\tau = u_e L_e / \nu \gg 10^4$ . Here  $u_e$  is a typical eddy velocity scale of order the friction velocity,  $u_*$ ;  $L_e$  is an eddy length scale above the surface layer, which was shown in HHS to be of about the same magnitude as the depth of the surface layer, and  $\nu$  is kinematic viscosity. With such high  $Re_\tau$ , the strain of the detached eddy is strong enough to overcome the shear in the surface layer. This is not the case for typical laboratory flow or in Direct Numerical Simulations (DNS) of neutral boundary layers, where  $Re_\tau < 10^3$  (Spalart, 1988; Robinson, 1991). For this class of flow, the shear in the surface layer is so strong (relative to the strain of detached eddies) that the shear sheltering effect (Hunt and Durbin, 1999) prevents eddies from above penetrating down to the surface. This results in the well-known situation with elongated streaks near the wall (e.g. Lee *et al.*, 1990; Adrian *et al.*, 2000) and upward bursting motions, which extend throughout the whole boundary layer and indeed dominate its outer structure (e.g. Adrian *et al.*, 2000).

In what follows, we will base our interpretation of the measurement results on the hypothesis that large-scale roller eddies and detached eddies may coexist or, depending on the value of  $L$ , one or the other mode may dominate.

## 5.2. Interpretation of the observational results

It is clear from the presentation of the measurement data in the previous section that there is a dramatic change in the dominant horizontal scale of the temperature fluctuations between the fully unstable and slightly unstable (UVCN) regimes. In the fully unstable regime (where  $L$  is of the order of the surface layer depth or less) the temperature scale is the same as that of the longitudinal wind fluctuations (i.e. comparable to the boundary layer thickness), Figure 6. In the UVCN regime, the length scale of temperature fluctuations becomes equivalent to the much smaller scale of the vertical velocity fluctuations, Figure 8. The co-spectral analysis also demonstrated that the corresponding length scale for vertical transport of temperature (or sensible heat) undergoes a similar reduction, Figures 10, 11 and 12.

In their study of organized structures in the near-neutral surface layer, Höögström and Bergström (1996) found that the mean duration of ‘bursts’ (negative  $u'$  and positive  $w'$ ) and ‘sweeps’ (positive  $u'$  and negative  $w'$ ) as well as the interval between such events was constant (i.e. independent of wind speed) for a given height in the surface layer and increasing systematically with height. The typical mean value for the duration of bursts and sweeps referred to  $z = 3$  m was about 5 seconds, whereas the corresponding interval between events was about 15 seconds. The duration of momentum transport events  $T$  is

approximately related to  $n_{\max}$ , the frequency of maximum in the  $uw$  co-spectrum, by

$$1/T \approx n_{\max}. \quad (21)$$

From the observations, Figure 12(c) and (d),  $f_{\max} = n_{\max} z / U \approx 0.06$ , i.e.  $T \approx 17z / U$ , which gives  $T \approx 7$  seconds for  $z = 3$  m and a typical wind speed of  $7 \text{ m s}^{-1}$ , which is in reasonable agreement with the observed values for the duration of the events and the intervals between them. Höögström and Bergström (1996) found that about 90% of the momentum flux was achieved by organized eddies of the size identified by the structure analysis in that paper.

Observed values for  $f_{\max}$  of the  $w\theta$  cospectra is about 0.3, which means that corresponding  $T$ -values are a factor 5 smaller. This illustrates that the heat transport mechanism in the UVCN range differs in a systematic way from the corresponding momentum transport both at the land site and the marine site.

The observed features of the dissipation of turbulent energy shown in Figure 3 and the corresponding mechanism for the dissipation of temperature fluctuations, Figure 4, are also consistent with the detached-eddy model. In the strong shear near the surface, a large proportion of the kinetic energy of the eddy is being dissipated. The variation with height of  $\phi_\varepsilon$  for  $z/L = 0$ ,  $\phi_{\varepsilon n}$ , shown in Figure 3, has not been noted in previous studies of the turbulence kinetic energy (TKE) budget of the surface layer. In the Kansas study, Wyngaard and Coté (1971) presented probably the first complete TKE analysis. But in that experiment, near-neutral conditions were obtained only during short, probably non-stationary periods. In fact, their plot of  $\phi_\varepsilon$  against  $z/L$  (their Figure 5) has no observations for the range  $-0.1 < z/L < 0$ , so the authors simply extrapolate their curve to the ‘expected’ value of  $\phi_\varepsilon = \phi_{\varepsilon n} = 1.0$  for  $z/L = 0$ . Höögström (1990) assumed MOST to be valid and found  $\phi_\varepsilon = 1.24$  for  $z/L = 0$  as a mean value from his measurements at 3, 6 and 13.9 m. Analysing data from the Laban’s mills site (i.e. the present ‘land’ site), Höögström (1992) still assumed MOST to be valid and concluded that  $\phi_{\varepsilon n} = 1.24$ . Oncley *et al.* (1990) reported, however,  $\phi_{\varepsilon n} = 0.80$ , and Frenzen and Vogel (1992) presented results from another surface-layer experiments giving  $\phi_{\varepsilon n} = 0.89$ . Considering the result of Figure 3, it is reasonable to conclude that this apparent controversy between previous authors is probably simply the result of using different measuring heights – this was certainly the case with the reference Höögström (1992), which was based on the same data that make up the ‘land’ data of Figure 3.

It is interesting to compare how data behave for small  $-z/L$ -values in the  $\phi_\varepsilon$ -plot, Figure 3 and in the corresponding plot for the temperature fluctuation dissipation  $\phi_{NT}$ , Figure 4. For  $\phi_\varepsilon$ , both the ‘land’ data for 6.3 m and the ‘sea’ data for 10 m are less than unity in this stability range, but the 1.6 m data at the ‘land’ site are much above unity. This indicates how turbulent kinetic energy

very close to the surface is transported downwards from higher levels in the surface layer above say 4 m above the ground. This enhances intense dissipation close to the surface. The corresponding plot for  $\phi_{NT}$  (Figure 4) displays a different picture in the UVCN range. The 10 m data at the ‘marine’ site are most conclusive, with values systematically much in excess of the values corresponding to local production, which for this level decreases rapidly for  $-z/L < 0.1$ . The data points representing the ‘land’ site are less conclusive, with large spread for both measurement heights (1.6 and 6.3 m). Consider, however, the finding of Figure 2 that the production term  $\phi_H$  decreases rapidly towards zero in the UVCN range. In this range  $\phi_{NT}$  clearly exceeds the value associated with local production. Also, in the UVCN range, temperature fluctuations are created mainly at heights well above 10 m and dissipated below that height, stressing the relative importance of downdraughts for the turbulent heat transport process at the surface, cf. further discussion below.

For an analysis of the heat flux mechanism in the UVCN regime, we start by noting that at both the land site and the marine site, when  $-L > 150$  m, MOST becomes invalid and  $\phi_H$  drops to small values. Thus the heat flux is much larger than would be expected from MOST. At the marine site, we observed this situation to be closely linked to the occurrence of a small sea/air temperature difference,  $\Delta\Theta = (\Theta_w - \Theta_{10}) < 1.7$  K. As shown in Figure 9 of SHSJ, for this value of  $\Delta\Theta$  a marked increase occurs in the heat transfer rate defined by the quantity  $y$  of Equation (22):

$$y = |T_*|/(\Theta_w - \Theta_{10}) = \frac{\overline{w'\theta'}}{u_*} / (\Theta_w - \Theta_{10}), \quad (22)$$

which, for the case of  $U_{10} > 10$  m s<sup>-1</sup>, is found to be much larger for  $\Delta\Theta < 1.7$  K than for  $\Delta\Theta > 1.7$  K (where it is essentially constant). Thus, in this near-neutral situation with small sea/air temperature difference ( $\Delta\Theta < 1.7$  K) and high wind speed ( $U_{10} > 10$  m s<sup>-1</sup>), surface layer scaling (i.e. MOST) is no longer valid when  $-L$  is larger than 150 m. This departure from MOST is greatest for the largest scale eddies, but it also affects the mean fluxes, as the above analysis demonstrates.

When MOST is strictly valid, a roughness length can be defined for temperature,  $z_{0T}$ . Then the ‘resistance’  $r_H$  to the temperature flux between the height  $z$  in the atmospheric surface layer and the surface defined by  $z = z_{0T}$  is given in terms of  $y$  by:

$$r_H(z, z_{0T}) = \frac{\Theta_{10} - \Theta_w}{-\overline{w'\theta'}} = \frac{1}{u_* y}. \quad (23)$$

Since, in ideal near-neutral conditions (MOST), the temperature profile is logarithmic,

$$r_H(z, z_{0T}) = \frac{\ln(z/z_{0T})}{ku_*}, \quad (24)$$

so that

$$y(z, z_{0T}) = \frac{k}{\ln(z/z_{0T})}. \quad (25)$$

But in the UVCN regime, when MOST is not valid, it is not possible to employ Equations (23)–(25) in a strict sense. Nevertheless, the equations can be used to derive an *apparent*  $z_{0T}$ -value for each of these cases as well (for some defined value of  $z$ ). Figure 16 of SHSJ shows that these  $z_{0T}$ -values (denoted by closed stars) are significantly higher than for neutral conditions for similar values of  $U_{10}$  (with weak convection where  $-L < 150$  m). It appears that the heat exchange mechanism in the UVCN regime is more effective than the ‘ordinary’ MOST mechanism. Our results show that this is an atmospheric dynamical process which is equally effective over land.

To understand these statistical results, it is helpful to consider how the eddy structure changes using these and other data, as well as theoretical models and numerical simulations. A notable feature in Figure 7, for the temperature spectrum at the marine site, as well as  $w\theta$  co-spectra at the marine and the land sites, shown in Figures 10 and 11 respectively, is a characteristic spectral shape with two peaks, separated by more than a decade in frequency, which occurs for  $40$  m  $< -L < 150$  m. These features may be interpreted as coexistence of elongated structures with length scales greater than the depth of the boundary layer (Figure 1(a)) and unsteady detached eddies (Figure 1(b)) that determine the moderate and smaller scale eddies in the strong mean shear in the surface layer. The structures vary considerably in how they affect the heat flux and temperature spectra. For the moderately convective case (Figure 14(a),  $-L = 6.3$  m) almost the entire heat flux is accomplished by upward motion of warm air, whereas for the UVCN case, Figure 14(b), there is a large additional contribution to the heat flux from downward motion of colder air. This leads to  $\phi_H$  decreasing, as shown in Figure 2. Our hypothesis is that, where detached eddy structures in the mixed layer impinge on the surface layer, they increase the heat flux. Thus the transport efficiency in the UVCN regime may be related to increased importance of downdraughts to the temperature flux. This is clearly illustrated in the quadrant analysis.

A conceptual model of eddies (Hunt and Durbin, 1999) impinging on thin shear layers shows how the thermal and velocity length scales might vary. Consider a typical detached vortical eddy, which may be idealised as a vortex ring, descending towards the surface shear layer near the ground and then, as it induces instabilities and small-scale fluctuations, mixes with the surface layer flow.

In the first stage, as the eddy impacts on the vorticity of the surface layer, it induces, outside the eddy, vertical and streamwise velocity fluctuations on a much greater length scale than that of the impinging eddy – as depicted in Figure 1(b). The thermal/concentration field within the eddy moves with the vorticity of the eddy and is not

initially stretched to the same extent as the perturbed velocity field in the surface layer. This finding is in qualitative agreement with the basic result of this study that the scale of the temperature fluctuations in the UVCN regime is much smaller than the corresponding scale for longitudinal wind component (Figure 8).

In the second phase, as the impinging eddy breaks up in the surface layer, it induces fluctuating Reynolds stresses as it interacts with the mean velocity gradient and correlated thermal and velocity fluctuations in the mean temperature gradient of the surface layer. Linear theory (Townsend, 1976, chapter 8) shows how, in this rapidly developing distortion, the eddy diffusivity for heat/mass transfer is about  $5/2$  times as great as for momentum (by comparison with fully developed shearing flows, where the ratio is close to unity). Although linear theory is a simplified model of this complex process, the result is in qualitative agreement with our finding that, in the UVCN regime,  $\phi_H$  is much less than  $\phi_m$  near the surface. When  $-L > 150$  m, shear processes in the bulk of the boundary layer and surface layer prevent the formation of large thermal structures, but the effect of shear on elongating surface eddies is still present (see also Dobrinski *et al.* 2004; Hanazaki and Hunt 2004), as we see in the  $u$ -spectra, Figure 8.

Another feature which corroborates the above conceptual model of the difference in the heat transport mechanism and the momentum transport mechanism for the UVCN regime is seen when comparing the figures for the dimensionless kinetic energy dissipation  $\phi_\epsilon$ , Figure 3, and the corresponding plot for the dimensionless dissipation of the temperature fluctuations  $\phi_{NT}$ , Figure 4. Whereas the  $\phi_\epsilon$ -plot clearly illustrates a process with local dissipation deficit at 6.3 and 10 m and strongly enhanced dissipation at 1.6 m, the  $\phi_{NT}$ -plot displays a process of deeper vertical extension, since in the UVCN regime, temperature dissipation is observed to be excessive at all measurement heights in the 1.6 to 10 m height range.

As noted in section 4.2, the anomalous behaviour of  $\phi_H$ , which is so evident at 10 m height at the marine site, is not found further above the ground at 17 and 26 m. This observed variation of the transport mechanism with height raises the question whether the observed anomaly may be due to spray effects over the ocean. The fact that features observed at 10 m over the sea agree very well with corresponding findings at the land site makes, however, this interpretation unlikely. Also, calculations with Andreas' (2004) spray model by Sahlée *et al.* (2007) showed conclusively, that for wind speeds less than  $14 \text{ m s}^{-1}$ , the spray effect on the heat fluxes is expected to be less than 10%. It is also important to stress that the bathymetry outside the measurement site Östergarnsholm is such that no violent breaking of waves takes place in front of the tower, causing possible 'showers' of drops onto the instrumentation at 10 m (at least not for winds well below  $20 \text{ m s}^{-1}$ ). It is also notable that the salinity of the Baltic Sea is only about 6 ppt. This fact makes it possible to rule out effects from salt contamination of

instruments often encountered in measurements over the deep sea, where the salinity is about 30 ppt.

The above discussion highlights the special transport process in the atmospheric surface layer in the UVCN regime, but it does not explain directly how this leads to decreasing resistance to the temperature flux at the sea surface. Surface renewal theory, Liu *et al.* (1979), requires that the transport of heat is accomplished solely by molecular conduction through the surface microlayer, but from Figure 16 of SHSJ, the observations show that  $z_{OT}$  starts to deviate from the curve representing surface renewal theory as soon as the wind speed exceeds about  $10 \text{ m s}^{-1}$ . As briefly discussed in SHSJ, it is clear from recent air–sea tank experiments and theoretical studies (several presentations at 37<sup>th</sup> International Liège Colloquium on Ocean Dynamics, 2–6 May 2005, 'Gas Transfer at Water Surfaces'; to be published in *J. Marine Systems*) that air–sea transfer is highly intermittent and that wave breaking plays a crucial role. It is likely that with increasing importance of intense downbursts, the frequency and intensity of wave breaking increases considerably, which in turn, leads to disruption of the surface microlayer. It is a reasonable interpretation of the results (Figure 16 of SHSJ) that this process starts to be effective as soon as the wind speed exceeds  $10 \text{ m s}^{-1}$ , and that the effectiveness of the process increases further in the UVCN regime. The observation from the marine site mentioned above that the UVCN regime in the present dataset is always associated with small air/sea temperature difference may also be a crucial factor for the effectiveness of heat transport during the highly episodic downburst events or, possibly, the result of the effectiveness of this transport.

## 6. Conclusions

Analysis of atmospheric surface layer data from a marine site and from a flat land site during conditions with relatively strong wind and upward flux of sensible heat of moderate magnitude has revealed the existence of a turbulence regime which we term 'the unstable very close to neutral regime' or the UVCN regime, which has properties that differ from the predictions based on surface layer theory (MOST). We find that the UVCN regime appears for  $-L > 150$  m (probably this criterion should rather be formulated in terms of  $h/L$ , where  $h$  is the height of the boundary layer, but this quantity was not included in the present dataset). The UVCN regime was found to have the following characteristics:

- (i) Below a height of approximately 15 m, the non-dimensional temperature gradient  $\phi_H$  decreases to small values as  $z/L$  decreases towards zero (instead of increasing towards a value close to one as expected from Monin–Obukhov theory).
- (ii) Close to the surface the non-dimensional dissipation of turbulent kinetic energy  $\phi_\epsilon$  is not in balance with local production, being much smaller than production at 6.3 and 10 m and much larger at 1.6 m.

- (iii) The non-dimensional rate of dissipation of the variance of temperature fluctuation is significantly larger than the local rate of production at all measuring heights between 1.6 m and 10 m.
- (iv) Temperature spectra have a length scale that agrees closely with that of corresponding spectra for the vertical velocity component, which is about 1/5 of the depth of the surface layer – in strong contrast to the case of moderate convection when the temperature spectra agree closely with the corresponding spectra for the longitudinal velocity component.
- (v) A larger proportion of the (upward directed) heat flux is associated with downbursts of cold air, than in moderately unstable conditions.

The observed features are interpreted as possible manifestations of a bifurcation of the large-scale eddy structure towards a state in which there are quasi-steady longitudinal rolls and, on a smaller scale, unsteady detached eddies. Our interpretation of the results from the measurements is that, in the UVCN regime, the latter component plays a significant role for the exchange of sensible heat. Thus, high-speed air from above the surface layer is engulfed into the surface layer and brought down to the surface as detached eddies. Linear theory (Townsend, 1976) predicts that for a field of such detached eddies, the eddy diffusivity for heat can be as great as 5/2 times that for momentum. This is consistent with our observations described in (i) above.

In the companion paper SHSJ, the analysis shows that, as long as the mean wind speed at 10 m is below about  $10 \text{ m s}^{-1}$ , the heat exchange mechanism at the water surface appears to be well described by classical 'surface renewal theory'. But for winds above  $10 \text{ m s}^{-1}$  in general and for the UVCN regime in particular, the roughness length for temperature increases significantly compared to predictions from 'surface renewal theory'. The interpretation is that wind gusts amplified by downdraughts play a crucial role in disrupting the laminar microlayer and hence decreasing the resistance to the heat flux at the surface.

Our observations indicate that the UVCN regime is of inherent dynamical origin and not specifically related to flow over waves. Over land, this regime is likely to occur in most cases during brief periods of limited climatological significance when the flow switches from slightly unstable to stable or vice versa. The situation over the sea at mid and high latitudes may be quite different, with the UVCN regime sometimes prevailing for long time periods. Climatically, the exchange of sensible heat may, however, often be of relatively minor importance compared to the corresponding exchange of latent heat. But as demonstrated in Sahl e *et al.* (2007), because the exchange of water vapour appears also to be enhanced in the UVCN regime, the results of these two papers suggest a possibly significant impact.

## Acknowledgements

This work was funded by The Swedish Research Council, grant no 621-2002-5348. We wish to thank Dr Hans Bergstr m and other colleagues at MIUU who are responsible for the measurements at  stergarnsholm. We also thank Dr Kimmo Kahma and Dr Heidi Pettersson from the Finnish Institute of Marine Research, Helsinki, Finland, for providing the wave buoy data. JCRH is grateful for the support of Cornell University while he was a Mary B Upson visiting Professor. We are grateful for conversations with Dr Harm Jonker at Delft.

## References

- Adrian RJ, Meinhart CD, Tomkins CD. 2000. Vortex organization in the outer region of the turbulent boundary layer. *J. Fluid Mech.* **422**: 1–54.
- Andreas EL. 2004. A bulk air-sea flux algorithm for high-wind, spray conditions, version 2.0. *Preprints, 13th Conference on Interactions of the Sea and Atmosphere, Portland, ME, 9–13 August 2004*. American Meteorological Society, CD-ROM P1.5.
- Benjamin TB. 1978. Bifurcation phenomena in steady flows of a viscous fluid. I. Theory. *Proc. R. Soc. London A* **359**: 1–26.
- Corrsin S. 1951. On the spectrum of isotropic temperature fluctuations in an isotropic turbulence. *J. Appl. Phys.* **22**: 469–473.
- Dobrinski P, Carlotti P, Newsom RK, Banta RM, Foster RC, Redelsperger J-L. 2004. The structure of the near-neutral atmospheric surface layer. *J. Atmos. Sci.* **61**: 699–714.
- Frenzen P, Vogel CA. 1992. The turbulent kinetic energy budget in the atmospheric surface layer: A review and an experimental reexamination in the field. *Boundary-Layer Meteorol.* **60**: 49–76.
- Guo Lars n X, Smedman A-S, H gstr m U. 2004. Air-sea exchange of sensible heat over the Baltic Sea. *Q. J. R. Meteorol. Soc.* **130**: 519–539.
- Hanazaki H, Hunt JCR. 2004. Structure of unsteady stably stratified turbulence with mean shear. *J. Fluid Mech.* **507**: 1–42.
- H gstr m U. 1988. Non-dimensional wind and temperature profiles in the atmospheric surface layer. *Boundary-Layer Meteorol.* **42**: 263–270.
- H gstr m U. 1990. Analysis of turbulence structure in the surface layer with a modified similarity formulation for near neutral conditions. *J. Atmos. Sci.* **47**: 1949–1972.
- H gstr m U. 1992. 'Further evidence of 'inactive' turbulence in the near neutral atmospheric surface layer.' Pp. 188–191 of Proceedings, AMS Tenth Symposium on Turbulence and Diffusion, Portland, Oregon, 29 Sept – 2 Oct 1992.
- H gstr m U, Bergstr m H. 1996. Organized turbulence structures in the near-neutral atmospheric surface layer. *J. Atmos. Sci.* **53**: 2452–2464.
- H gstr m U, Hunt JCR, Smedman A-S. 2002. Theory and measurements for turbulence spectra and variances in the atmospheric neutral surface layer. *Boundary-Layer Meteorol.* **103**: 101–124.
- Holmes P, Lumley JL, Berkooz G. 1996. *Turbulence, coherent structures, dynamical systems and symmetry*. Cambridge University Press.
- Hunt JCR, Carlotti P. 2001. Statistical structure at the wall of the high Reynolds number turbulent boundary layer. *Flow, Turbulence and Combustion* **66**: 453–475.
- Hunt JCR, Durbin PA. 1999. Perturbed vortical layers and shear sheltering. *Fluid Dyn. Res.* **24**: 375–404.
- Hunt JCR, Morrison JF. 2000. Eddy structure in turbulent boundary layers. *Eur. J. Mech. B/Fluids* **19**: 673–694.
- Johansson C, Smedman A-S, H gstr m U, Brasseur JG, Khanna S. 2001. Critical test of the validity of Monin–Obukhov similarity during convective conditions. *J. Atmos. Sci.* **58**: 1549–1566.
- Kaimal JC, Wyngaard JC, Izumi Y, Cot  OR. 1972. Spectral characteristics of surface-layer turbulence. *Q. J. R. Meteorol. Soc.* **98**: 563–589.
- Khanna S, Brasseur JG. 1998. Three-dimensional buoyancy- and shear-induced local structure of the atmospheric boundary layer. *J. Atmos. Sci.* **55**: 710–743.
- Lee MJ, Kim J, Moin P. 1990. Structure of turbulence at high shear rate. *J. Fluid Mech.* **216**: 561–583.

- Liu WT, Katsaros KB, Businger JA. 1979. Bulk parameterization of air-sea exchanges of heat and water vapor including the molecular constraints at the interface. *J. Atmos. Sci.* **36**: 1722–1735.
- Lu SS, Willmarth WW. 1973. Measurements of the structure of the Reynolds stress in a turbulent boundary layer. *J. Fluid Mech.* **60**: 481–511.
- Mason PJ, Sykes RI. 1982. A two-dimensional numerical study of horizontal roll vortices in an inversion capped planetary boundary layer. *Q. J. R. Meteorol. Soc.* **108**: 801–823.
- Monin AS. 1950. Turbulence in the atmospheric surface layer. *Coll. Sci. Inf. Hydrometeor. Ser. USSR* **1**: 13–27.
- Monin AS, Obukhov AM. 1953. Dimensionless characteristics of turbulence in the atmospheric surface layer. *Dok. AN SSSR* **93**: 223–226.
- Monin AS, Obukhov AM. 1954. Basic laws of turbulent mixing in the ground layer of the atmosphere. *Tr. Geofiz. Akad. Nauk. SSSR* **151**: 163–187.
- Obukhov AM. 1946. Turbulence in a thermally inhomogeneous atmosphere. *Trudy In-ta Teoret. Geofiz. AN SSSR* **1**: 95–115. English translation in: *Boundary-Layer Meteorol.* **2**: 7–29.
- Oncley SP, Businger JA, Itsweire EC, Friehe CA, LaRue JC, Chang SS. 1990. 'Surface layer profiles and turbulence measurements over uniform land under near-neutral conditions.' Pp. 237–240 in Proceedings from AMS Ninth Symposium on Turbulence and Diffusion, April 30 – May 3, 1990, Roskilde, Denmark.
- Raupach MR. 1981. Conditional statistics of Reynolds stress in rough-wall and smooth-wall turbulent boundary layers. *J. Fluid Mech.* **108**: 363–382.
- Robinson SK. 1991. 'The kinematics of turbulent boundary layer structure.' NASA Tech. Memo. 103859, Ames Research Center, Moffet Field, California.
- Sahlée E, Smedman A-S, Högström U, Rutgersson A. 2007. Bulk exchange coefficient for humidity at sea during unstable and neutral conditions: A re-evaluation based on new field data. *J. Phys. Oceanogr.* submitted.
- Smedman A, Guo Larsén X, Högström U, Kahma KK, Pettersson H. 2003. Effect of sea state on the momentum exchange over the sea during neutral conditions. *J. Geophys. Res.* **108**(C11): 3367, doi: 10.1029/2002JC001526.
- Smedman A-S, Högström U, Sahlée E, Johansson C. 2007. Critical re-evaluation of the bulk transfer coefficient for sensible heat over the ocean during unstable and neutral conditions. *Q. J. R. Meteorol. Soc.* **133**: [this issue].
- Spalart PR. 1988. Direct simulation of a turbulent boundary layer up to  $Re_\theta = 1410$ . *J. Fluid Mech.* **187**: 61–98.
- Sreenivasan KR. 1996. The passive scalar spectrum and the Obukhov–Corrsin constant. *Phys. Fluids* **8**: 189–196.
- Stull RB. 1988. *An introduction to boundary layer meteorology*. Kluwer Academic Publishers: Dordrecht/Boston/London.
- Townsend AA. 1976. *The structure of turbulent shear flow*. Second edition. Cambridge University Press.
- Warhaft Z. 2000. Passive scalars in turbulent flows. *Annual Rev. Fluid Mech.* **32**: 203–240.
- Willmarth WW, Lu SS. 1974. Structure of the Reynolds stress and the occurrence of bursts in the turbulent boundary layer. *Adv. Geophys.* **18A**: 287–314.
- Wyngaard JC, Coté OR. 1971. The budgets of turbulent kinetic energy and temperature variance in the atmospheric surface layer. *J. Atmos. Sci.* **28**: 190–201.